

Chemical Equilibrium Abundances in Brown Dwarf and Extrasolar Giant Planet Atmospheres

Adam Burrows¹ & C.M. Sharp¹

Received _____; accepted _____

June 29, 2021

arXiv:astro-ph/9807055v1 6 Jul 1998

¹Department of Astronomy and Steward Observatory, The University of Arizona, Tucson,
AZ 85721

ABSTRACT

We calculate detailed chemical abundance profiles for a variety of brown dwarf and extrasolar giant planet atmosphere models, focusing in particular on Gliese 229B, and derive the systematics of the changes in the dominant reservoirs of the major elements with altitude and temperature. We assume an Anders and Grevesse (1989) solar composition of 27 chemical elements and track 330 gas-phase species, including the monatomic forms of the elements, as well as about 120 condensates. We address the issue of the formation and composition of clouds in the cool atmospheres of substellar objects and explore the rain out and depletion of refractories. We conclude that the opacity of clouds of low-temperature (≤ 900 K), small-radius condensibles (specific chlorides and sulfides, not silicates), may be responsible for the steep spectrum of Gliese 229B observed in the near infrared below $1 \mu\text{m}$. Furthermore, we assemble a temperature sequence of chemical transitions in substellar atmospheres that may be used to anchor and define a sequence of spectral types for substellar objects with T_{eff} s from ~ 2200 K to ~ 100 K.

1. Introduction

After a decade of ambiguous detections, bona fide brown dwarfs and extrasolar giant planets (EGPs; Burrows *et al.* 1995) are now being discovered at an accelerating pace. Whether by radial velocity techniques (Mayor & Queloz 1995; Marcy & Butler 1996; Butler & Marcy 1996; Latham *et al.* 1989; Cochran *et al.* 1997), by direct detection in the field (Tinney, Delfosse, & Forveille 1997; Delfosse *et al.* 1998; Tinney *et al.* 1998 (DENIS); Kirkpatrick, Beichman, & Skrutskie 1997; Kirkpatrick *et al.* 1998 (2MASS)), by direct detection in young stellar clusters (Zapatero-Osorio, Rebolo, & Martin 1997; Comeron *et al.* 1993), by direct detection around nearby stars (Nakajima *et al.* 1995; Oppenheimer *et al.* 1995; Matthews *et al.* 1996; Oppenheimer *et al.* 1998 (Gl 229B)), or from space (Terebey *et al.* 1998 (NICMOS)), the expanding census of objects beyond the solar system with masses between $0.5 M_J$ and $80 M_J$ is lending new urgency to theoretical efforts to understand their evolution, spectra, and compositions.¹ At the low temperatures ($100 \text{ K} \leq T \leq 2500 \text{ K}$) achieved in the dense, high-gravity atmospheres of brown dwarfs and EGPs, chemical species not encountered in traditional stellar realms assume a new and central importance.

The molecular compositions of these exotic, low-ionization atmospheres can serve as diagnostics of temperature, mass, and elemental abundance and can help define a spectral sequence, just as the presence or absence of spectral features associated with various ionization states of dominant, or spectroscopically active, atoms and simple molecules does for M through O stars. However, the multiplicity of molecules that appear in their atmospheres lends an additional complexity to the study of substellar mass objects that is both helpfully diagnostic and confusing. Nowhere is the latter more apparent than in the

¹ M_J is the mass of Jupiter and is equal to $\sim 9.55 \times 10^{-4} M_\odot$.

appearance at low temperatures of refractory grains and clouds. These condensed species can contribute significant opacity and can alter an atmosphere’s temperature/pressure profile and its albedo. Grain and cloud droplet opacities depend upon the particle size and shape distribution and these are intertwined with the meteorology (convection) in complex ways. Furthermore, condensed species can rain out and deplete the upper atmosphere of heavy elements, thereby changing the composition and the observed spectrum. Hence, in brown dwarf and EGP atmospheres, abundance and temperature/pressure profiles, particle properties, spectra, and meteorology are inextricably linked.

One might naturally throw up one’s hands at the messiness of this problem were it not for two things: 1) there are chemical systematics that somewhat simplify the study of these atmospheres and 2) further progress in understanding the edge of the main sequence, brown dwarfs, and EGPs hinges directly upon its resolution. The goal of this paper is to explore and clarify the chemical condensation sequences, molecular abundance profiles, and molecular spectral diagnostics of brown dwarf and EGP atmospheres.

The formation of refractory silicate grains below 2500 K was already shown by Lunine *et al.* (1989) and Burrows *et al.* (1989) to influence the evolution of late M dwarfs and young brown dwarfs through their “Mie” opacity. The blanketing effect they provide lowers the effective temperature (T_{eff}) and luminosity (L) of the main sequence edge mass from about 2000 K and $10^{-4} L_{\odot}$ to about 1750 K and $6 \times 10^{-5} L_{\odot}$, an effect recently verified by Chabrier *et al.* (1998). In addition, grain opacity slightly delays the cooling of older brown dwarfs, imprinting a slight bump on their luminosity/age trajectories (see Figure 7 of Burrows *et al.* 1997). The presence of grains in late M dwarf spectra was invoked to explain the weakening of the TiO bands and the shallowing of their H₂O troughs in the near infrared (Tsuji *et al.* 1996; Jones & Tsuji 1997). Tsuji and collaborators concluded that titanium was being depleted into refractories, a conclusion with which we agree (see §3).

Gl 229B (Nakajima *et al.* 1995; Oppenheimer *et al.* 1998) is a Rosetta stone for brown dwarf research. With a T_{eff} of ~ 950 K, a luminosity below $10^{-5} L_{\odot}$, and spectra or photometry from the *R* Band through $5 \mu\text{m}$, Gl 229B hints at or exemplifies all of the unique characteristics of the family (Marley *et al.* 1996; Allard *et al.* 1996): metal (Fe, Ti, V, Ca, Mg, Al, Si) depletions, the dominance of H_2O vapor, the appearance of CH_4 and alkali metals, and the signatures of clouds. Clouds of low-temperature condensible species above the photosphere are the most natural explanation for the steep drop below $1 \mu\text{m}$ in the Keck spectra between $0.83 \mu\text{m}$ and $1 \mu\text{m}$ (Oppenheimer *et al.* 1998). These clouds may not be made up of the classic silicate refractories formed at much higher temperatures, since these species have probably rained out (Marley *et al.* 1996). From simple Mie theory, their mean particle size must be small ($\sim 0.2 \mu\text{m}$) in order to influence the “optical” without much perturbing the near infrared. In addition, such a population of small droplets can help explain why Gl 229B’s near-infrared troughs at $1.8 \mu\text{m}$ and $3.0 \mu\text{m}$ are not as deep as theory would otherwise have predicted. Just as Tsuji and collaborators have shown that silicate grains at higher temperatures can shallow out the H_2O troughs, so too can species that condense at lower temperatures (≤ 1000 K ?) explain the shallower-than-predicted Gl 229B H_2O troughs. What those species might be can be illuminated by chemical abundance studies and is one of the subjects of this paper. Note that a cloud grammage in these small-radius low-temperature refractories of only $\sim 10^{-5} \text{ gm cm}^{-2}$ would be adequate to explain the anomalies.

With Gl 229B as a reference benchmark, we explore the composition profiles of low-temperature brown dwarfs and EGPs to derive the systematics of the changes in the dominant reservoirs of the major elements (Table 1). These equilibrium chemical sequences are predominantly a function of temperature and can help to define a spectral sequence for substellar objects from the main sequence edge near 2000 K to EGPs with T_{eff} s of a few hundred Kelvin. The appearance and disappearance of various molecules and refractories

delineates an effective temperature sequence and the new proposed “L” dwarf spectral classification (Kirkpatrick *et al.* 1998) may correspond to a subset of the compositional sequences we derive.

However, as mentioned above, the full problem requires that the composition profiles, opacities, meteorology, temperature/pressure profiles, and spectra be handled self-consistently. At the present time, given the ambiguities in the grain/cloud properties and the paucity of optical constants, such a program is not realistic. In lieu of this, we employ the temperature/pressure profiles derived in Burrows *et al.* (1997). This allows us to define the overall trends, while at the same time focusing on the essential chemistry. The models of Burrows *et al.* (1997) consistently incorporate the abundances of the major gas-phase species, with their opacities, but do not include the thermal effects of the low-temperature condensibles. Nevertheless, the thermal profiles below the photospheres (at higher pressures) are always close to adiabatic, while the thermal profiles at lower optical depths are generally super-adiabatic ($|dT/dr|$ small). Coolants in the atmosphere and non-gray effects generally lower the temperatures achieved at the lower pressures far below the Milne temperature ($\sim 0.81T_{\text{eff}}$) to near $\sim 0.5T_{\text{eff}}$. This has the consequence that species that would not otherwise condense in Gl 229B-like atmospheres may in fact be present. The Burrows *et al.* (1997) models incorporate such cooling and non-Eddington effects. In §2, we describe the techniques and procedures we employ to perform the equilibrium calculations. In §3, we present temperature profiles for representative model brown dwarf and EGP atmospheres. We also calculate various composition boundaries in temperature–pressure space between the major compounds of the abundant elements. In addition, element by element we describe the abundance profiles in realistic brown dwarf/EGP model atmospheres. This is the central section of the paper. In §4, we explore the potential effects of rainout and depletions on the remaining mix of dominant chemical species. In §5, we summarize the list and order, as a function of temperature, of chemical

indicators that can help to define a spectral classification scheme for substellar objects and we review our general findings.

2. Techniques, Algorithms, and Procedures

Using the brown dwarf and giant planet model atmospheres of Burrows *et al.* (1997), and assuming an Anders and Grevesse (1989) solar composition of the 27 chemical elements H, He, Li, C, N, O, F, Ne, Na, Mg, Al, Si, P, S, Cl, Ar, K, Ca, Ti, V, Cr, Mn, Fe, Co, Ni, Rb and Cs, we calculate the abundances of each of about 330 gas-phase species, including the monatomic forms of the elements, and of about 120 specified condensates. These calculations are performed at each of about 2000 temperature-pressure points for every atmosphere model.

Table 1 lists the abundances by number for the 27 elements used in these calculations. With the exception of lithium, rubidium and cesium, the list covers nearly all the most abundant elements anticipated to be in brown dwarf atmospheres. Lithium is added because it is an important brown dwarf indicator. Rubidium and cesium are added because they have recently been detected in cool objects (Oppenheimer *et al.* 1998; Tinney *et al.* 1998). Their very low excitation and ionization potentials make them good temperature indicators in a range where many other elements are associated into molecules or have condensed out.

The same methods were used as in Sharp and Huebner (1990), but the improved version of the original computer code SOLGASMIX (Besmann 1977) used in that paper was further improved in the current work by including more species, incorporating a number of error traps, and adding features to make the code more user-friendly. Using the multi-dimensional Newton-Raphson method of White, Johnson and Dantzig (1958), the equilibrium abundances of gas-phase and condensed-phase species at a given temperature,

pressure, and elemental composition were obtained by minimizing the total free energy of the system. After subtracting the constraint equation in the manner of Lagrange’s method of undetermined multipliers and linearizing, SOLGASMIX uses Gaussian elimination with pivoting to iteratively solve the resulting matrix equations. The free energy of each species at a particular temperature is obtained by evaluating a polynomial of the form

$$\Delta G_{\phi i}(T) = \frac{a}{T} + b + cT + dT^2 + eT^3, \quad (1)$$

where a , b , c , d and e are fitted coefficients and $\Delta G_{\phi i}(T)$ is the Gibbs free energy of formation at temperature T of species i in phase ϕ , relative to its constituent atoms in their monatomic neutral gaseous state. For instance, for H_2S the reference states of the elements are monatomic hydrogen and sulfur in the gas phase, whose energies of formation are zero by definition. If the species being considered is in the gas phase and is monatomic, all the coefficients on the right hand side of eq. (1) are zero.

In the original work of Sharp and Huebner (1990), the total free energy of the system was expressed quite generally in terms of the gas phase, several liquid or solid solutions (each containing at least two species), and distinct condensed phases of invariant stoichiometry (each containing a single species). In our current work, because of the large number of species considered, we decided to simplify the calculations and omitted solutions, such as the solid solution of melilite ($\text{Ca}_2\text{Al}_2\text{SiO}_7$ with $\text{Ca}_2\text{MgSi}_2\text{O}_7$). Thus, given a value of $\Delta G_{\phi i}(T)$ from eq. (1) for each chemical species, the elemental composition, and initial trial values of the species abundances, the total equilibrium free energy of the system is found by minimizing

$$\frac{G(T)}{RT} = \sum_{i=1}^m \left[n_{\phi i} \left\{ \frac{\Delta G_{\phi i}(T)}{RT} + \ln P + \ln \left(\frac{n_{\phi i}}{N} \right) \right\} \right]_{\phi=1} + \frac{1}{RT} \sum_{\phi=2}^{s+1} \left[n_{\phi i} \Delta G_{\phi i}(T) \right]_{i=1}, \quad (2)$$

where R is the gas constant, P is the total pressure in atmospheres, and N is the total number of moles in the gas phase. The first sum is over m species in the gas phase with $\phi = 1$, the second sum is over s condensed phases (numbered 2 to $s + 1$), and $n_{\phi i}$ is the number of moles of species i in phase ϕ . Each condensed phase is in fact only a single species, so $i = 1$ in the second sum, since we need to distinguish between, for example, $\text{H}_2\text{O}(\text{gas})$ and $\text{H}_2\text{O}(\text{liquid})$, which are considered separate species. The subsidiary mass balance relations are satisfied for each element j of the total number of elements, k , as follows:

$$\sum_{i=1}^m [\nu_{\phi ij} n_{\phi i}]_{\phi=1} + \sum_{\phi=2}^{s+1} [\nu_{\phi ij} n_{\phi i}]_{i=1} = b_j \quad \text{for } j = 1 \text{ to } k, \quad (3)$$

where $\nu_{\phi ij}$ is the stoichiometric coefficient of element j in species i in phase ϕ and b_j is the number of gram-atoms of element j . As in eq. (2), the first sum is over the gas-phase species ($\phi = 1$) and the second sum is over all the single component ($i = 1$) condensates.

Most of the thermodynamic data were obtained from the JANAF tables (Chase 1982; Chase *et al.* 1985). Data on a number of condensates not available in these tables were obtained from Turkdogan (1980) and data on the two condensates $\text{NaAlSi}_3\text{O}_8$ (high albite) and KAlSi_3O_8 (high sanidine) were obtained from Robie and Waldbaum (1968). Tsuji (1973) was the source of data for the gas-phase molecules CaH , CrH , MnH , NiH , MnO , NiO , MnS , TiS , TiN , SiH_2 , SiH_3 , together with some carbides of little importance in the brown dwarf context. Our database currently holds information on 1662 species, of which about 450 are followed in these calculations. For those species for which the JANAF tables were used, the coefficients in eq. (1) were obtained from a database generated in Sharp and Huebner (1993), in which the free energies were renormalized relative to the monatomic gaseous phase of each element, rather than relative to standard reference states. A polynomial with up to five coefficients as in eq. (1) was fitted over the tabulated

temperature range of each species. Using the redefined free energies has the advantage of removing any discontinuities associated with phase changes in the reference states, permitting polynomial fits to be made over large temperature ranges.

In Sharp and Huebner (1990), the only alkali elements considered were sodium and potassium, together with their most important compounds. In this work, we include all the other alkali elements, except francium, together with their most important compounds, in particular their chlorides and fluorides, in both gas and condensed phases. With the exception of rubidium, all the data were obtained from the JANAF tables. As no useful data on rubidium and its compounds are available in the JANAF tables, including in the more recent compilations in Chase *et al.* (1985), we used Barin (1995).

The JANAF tables are deficient in a number of important volatile condensates, the most important being $\text{H}_2\text{O}(\text{ice})$. A prescription for water from Eisenberg and Kauzmann (1969) was modified and incorporated into our code. A second important volatile condensate is $\text{NH}_3(\text{ice})$. The pure liquid phase of NH_3 , together with a number of its hydrated liquid phases, were not considered. The data for NH_3 were obtained from the CRC Handbook (Weast and Astle 1980) in the form of vapor pressure coefficients. Another important volatile condensate is ammonium hydrogen sulfide, NH_4SH , which is believed to be an important component in the Jovian atmosphere (Lewis 1969). As with $\text{NH}_3(\text{ice})$, we obtained the data for NH_4SH from the CRC Handbook, in the form of vapor pressure coefficients. However, unlike either NH_3 or H_2O , which on vaporization remain the same compound, NH_4SH decomposes into the two gaseous components, NH_3 and H_2S . In addition, we added NH_4Cl , which decomposes into NH_3 and HCl , but this species proves to be unimportant at the temperatures and pressures encountered in giant planet and brown dwarf atmospheres. Except for the data originating from Tsuji (1973) and our newly added data on the condensed phases of H_2O , NH_3 , NH_4SH , and NH_4Cl , which were expressed in

different forms, all data were converted to the same form as eq. (1), before the evaluation of eqs. (2) and (3). Furthermore, we replaced the polynomial fit for the gaseous species CO found in the JANAF tables with a polynomial fit based on its spectroscopic constants, as the spectroscopic data are very well known for this molecule (Sharp 1985).

We assume that the gas is ideal, *i.e.* that the activity of each species is the same as the partial pressure in atmospheres and, with the exception of liquid H₂O, only solid condensates are included in the calculations. We consider the neglect of the liquid phases to be quite reasonable, as the difference between the free energies of formation of the liquid and solid phase of a species is generally much smaller than the difference between the free energies of one of the condensed phases and the gas phase. For example, for iron in the range 1000 to 2000 K, the change in the free energy when converting the vapor into the liquid is at least five orders of magnitude larger than the corresponding change when converting the liquid to the solid. In the case of TiO, the ratio of the change in the free energy between vapor and liquid to between liquid and solid is much smaller, but is still at least one order of magnitude in the same range (though in detailed calculations other condensed oxides form). Additionally, the inclusion of ionization slows down the calculations substantially in any temperature region which involves both marginal ionization and condensation, as is the case in this work, and since ionized species play a negligible role at the lower temperatures of substellar atmospheres, we omit them.

The main object of this work is to derive the detailed equilibrium abundance profiles for models of the atmospheres of cool brown dwarfs and giant planets, given their temperature-pressure profiles, with particular reference to the brown dwarf Gliese 229B (Nakajima *et al.* 1995). Since we start with temperature-pressure profiles with specified gravities and effective temperatures from Burrows *et al.* (1997), to obtain such profiles for given ages and masses, we interpolate using the evolutionary calculations from that

work. Given a profile corresponding to the require model, we calculate the abundances by minimizing the free energy of the system. Starting at the high temperature end of the profile, the code uses approximate trial values based on the element abundances to start the calculations. Upon convergence, the abundances of selected species are written to a file for later graphical treatment. These abundances are then used as trial values for the next calculation 1 Kelvin lower in temperature, and at selected temperature intervals, typically 100 K, additional data are printed out. This process is repeated for progressively lower temperatures and pressures in the atmosphere, until the end of the data file is reached. At the high temperature end, convergence is usually rapid, since the gas consists of atomic and simple molecular species, and few, if any, condensates. At progressively lower temperatures, as more species condense out and the chemistry becomes more complicated, convergence is slower and more “delicate.” If the starting values before each iteration are too far away from the solution, there is a risk of non-convergence. It is for this reason that the calculations are always started at the high temperature end of a profile.

However, even with the above method, convergence problems can arise. It is found that between 1100 and 1200 K for pressures less than about 0.1 atmospheres the program may fail to converge. For higher pressures, the code generally operates successfully until temperatures below 600 K are reached. In the first case, non-convergence is often associated with the refractory condensate $\text{Ca}_2\text{MgSi}_2\text{O}_7$, and in the second case it is often associated with the less refractory (and very low abundance) condensate LiAlO_2 . In both cases, these condensates appear at higher temperatures, only to disappear into other species before the problems are encountered. Upon removal of these and many other similar species, such as Al_2O_3 , which is present only above about 1800 K in most models and disappears into other aluminum-bearing species at lower temperatures, the problems are often solved. These problems are caused by a too rapid change in abundance associated with condensation or a phase change. Unfortunately, it is often not possible without doing the calculations to know

ab initio which species are likely to be unimportant and can be neglected. Fortunately, removing gas-phase species of negligible abundance can speed up the calculations. After removing redundant species, iterations can be restarted.

If it was still not possible to obtain successful convergence after removing one or more redundant species, condensates that are present, but that can be considered inert, can be removed from the calculations, which can be restarted with trial values from a previous dump file. In the process of removing a condensate from the calculations, the corresponding abundances of each element tied up in the species is removed. For example, if the condensate spinel, MgAl_2O_4 , is present and is to be removed from the calculations, then given $N(\text{Mg})$ and $n(\text{MgAl}_2\text{O}_4)$, which are, respectively, the number of gram-atoms of Mg in all forms in the calculations and the number of moles of spinel, the corrected total abundance of Mg is $N(\text{Mg}) - n(\text{MgAl}_2\text{O}_4)$, that of Al is $N(\text{Al}) - 2n(\text{MgAl}_2\text{O}_4)$, and that of O is $N(\text{O}) - 4n(\text{MgAl}_2\text{O}_4)$, from which the relative element abundances can be obtained.

However, it was often found that at a lower temperature, removing a condensate changed the chemistry. A very good example is iron, which in our calculations normally forms the solid metal at high temperatures. If iron is retained in the calculations, at 718 K iron metal reacts with H_2S to form FeS , which is then the main compound of sulfur, and substantially depletes sulfur from the gas phase. If iron is removed from the calculations when it initially condenses, much more sulfur remains in the gas phase, which is then available to form the volatile condensate, NH_4SH , at lower temperatures. Hence, the presence of NH_4SH clouds inferred in Jupiter's atmosphere may be an indirect consequence of the rainout of iron metal to deeper regions.

3. Composition Boundaries and Abundance Profiles

Figure 1 depicts temperature–pressure profiles for 5, 10, 20, and 40 M_J atmosphere models from Burrows *et al.* (1997), for ages of 0.1, 1.0, and 10.0 Gyrs. Only the 5 and 10 M_J models are given at 0.1 Gyr. The dots identify the positions of the photospheres. This set of profiles represents the general trends in brown dwarfs and EGPs. Note that the concept of a photosphere is ambiguous, since the opacities are stiff functions of wavelength. Radiation at different wavelengths decouples from a variety of disparate pressure levels. By photosphere we mean here the level at which the temperature equals the effective temperature, defined via Stefan’s Law. This approach provides us with a sensible average position, but should not be overinterpreted.

Higher–mass models generally reside at higher entropies, *i.e.*, at a given temperature level the gas is at lower pressures. However, as Figure 1 demonstrates, cooling in the radiative zones above the photosphere at lower temperatures can result in a reversal of this behavior. Furthermore, for a given mass the older a substellar object the lower the effective temperature and the higher the photospheric pressure. In addition, for a given age the higher the mass the higher the photospheric pressure. However, and importantly, although the effective temperature is a strong function of age and mass, the corresponding pressure at the photosphere is only weakly dependent upon these quantities, and varies within \sim half a dex of 1 atmosphere. Consequently, the abundances of species at the photosphere of a brown dwarf or EGP are governed almost entirely by the temperature. This is an important conceptual simplification.

Figures 2 through 4 depict the regions of transition from one chemical species to another in temperature–pressure space for a variety of important constituents of equilibrium substellar atmospheres. Anders & Grevesse (1989) solar abundances are assumed (Table 1). Only a subset of the calculated and interesting composition boundaries are depicted.

Nevertheless, these figures summarize some of the diagnostic chemical sequences and transitions encountered in theoretical substellar atmospheres and the reservoirs of the major elements. Superimposed on these plots are atmospheric profiles of 5, 10, 20, and 40 M_J models at 1 Gyr from Figure 1. Also shown for comparison on Figures 2 through 4 are adiabats above and below the photospheres for more massive M dwarf models of Burrows *et al.* (1993) at 0.08, 0.09, and 0.115 M_\odot and 1 Gyr. As demonstrated in Figure 1, for a broad range of objects and ages, the narrow band around 1 atmosphere is relevant when looking at the compositions near the photosphere. Furthermore, the near verticality of the transition curves confirms that composition is most closely linked with temperature.

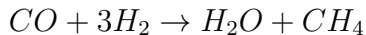
Figures 5 through 14 depict theoretical chemical equilibrium composition profiles versus temperature for Gl 229B–like models (see Marley *et al.* 1996; Allard *et al.* 1996) as a function of T_{eff} and gravity. To avoid confusion, only a subset of the major compounds are included in the plots. Implicit are the corresponding pressures from the atmosphere models of Burrows *et al.* (1997). The odd–numbered figures depict the gravity dependence for $T_{\text{eff}} = 950$ K and the even–numbered figures depict the T_{eff} dependence for a gravity of 1000 m s^{-2} . The figures are approximately in order of decreasing elemental abundance. Hence, Figures 5 through 14 and the curves on those figures follow the rough sequence: O, C, N, Mg, Si, Fe, S, Al, Ca, Na, P, K, Ti, V, Li, Rb, and Cs. We will describe each of these figures in turn, but even though they depict the range of theoretical abundance profiles for Gl 229B models, they demonstrate that the sequence of chemical reservoirs of the major elements as a function of temperature varies little with model. This is a consequence of the weak pressure and gravity dependence of the equilibrium abundances and the steepness of the transition boundary curves in Figures 2 through 4 relative to the model temperature–pressure profiles. Hence, the sequence of dominant chemical species for an element along the entire brown dwarf/EGP continuum and the transition temperatures from one species to another are very approximately universal. Note that the proximity

of a species to the photosphere and its importance in the emergent spectrum does vary importantly as a function of age and mass or gravity and T_{eff} . Tables 2a and 2b provide useful lists of the major chemical species of each of the most abundant elements found in the atmospheres of substellar objects.

3.1. Oxygen, Carbon, Nitrogen, Iron, Chromium, Sulfur, Titanium, Vanadium

As Figures 5 and 6 demonstrate, the major reservoir for oxygen in substellar atmospheres is gaseous H_2O . The only significant competitor for abundant oxygen is CO, but CO is converted into CH_4 between temperatures of 1100 and 2000 K. Only at temperatures below ~ 300 K does H_2O condense, as the liquid above 273.15 K, otherwise as ice. As is well known (Fegley & Lodders 1996), Jupiter has condensed H_2O below its photosphere. As is not so well known and as is demonstrated in Figure 2, at 1 Gyr a $10 M_J$ object may have condensed H_2O in its atmosphere. In fact, as Figure 2 suggests, all but the youngest EGPs and those not at elevated temperatures due to proximity to a primary (*e.g.*, 51 Peg b, τ Boo b) should have water clouds (Burrows *et al.* 1997). This may importantly affect their albedos and reflected spectra (Marley *et al.* 1998).

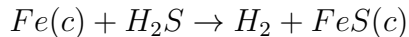
As alluded to above and as shown in Figures 5 and 6, the major reservoirs of carbon are CO and CH_4 . The reaction



and Le Chatelier’s Principle indicate that for a given temperature CO is favored at low pressures and gravities. CO is also favored at high temperatures and for models with high T_{eff} s. From Figures 5 and 6, it is expected that in Gl 229B CO will convert into CH_4 between temperatures of 1300 and 1800 K, depending upon T_{eff} and gravity. To put equilibrium CO closer to the photosphere in Gl 229B, high T_{eff} s and lower gravities are

preferred. This makes the interpretation of the detection in Gl 229B of CO at $4.67 \mu\text{m}$ (Noll, Geballe, & Marley 1997) problematic, since CO is not expected in great abundance near the photosphere for T_{eff} s near 950 K. This may imply that the higher CO abundances at the higher temperatures at depth are being advected out of equilibrium into the cooler regions of the photosphere and that the kinetics of the reaction might have to be considered. Be that as it may, CH_4 should be the major atmospheric reservoir of carbon for all but the youngest and hottest ($T_{\text{eff}} \geq 1300 \text{ K}$) brown dwarfs and EGPs.

Nitrogen is in the form of N_2 for temperatures above 800 K, but is converted into NH_3 between 600 and 800 K (Figures 5 and 6). From Figure 2, we see that the NH_3/N_2 boundary coincides with the typical atmospheric pressure level (~ 1 atmosphere) near the $\text{Fe} \rightarrow \text{FeS}$ transition. This flags the $\sim 700 \text{ K}$ level in a substellar object as another interesting transition. From Figures 2, 7 and 8, we see that for iron the first condensate to form (at $\sim 2200 \text{ K}$) is the metal, followed at much lower temperatures by the solid sulfide, FeS. FeH should also be present in abundance, but is not in our calculations (Fegley & Lodders 1996). The major reservoir for sulfur above 718 K is gaseous H_2S . As Guillot *et al.* (1997) have shown, at lower temperatures ZnS forms. Note that though $\text{Na}_2\text{S} (c)$ and $\text{K}_2\text{S} (c)$ are in our calculations, they never appear in great abundance (see §3.2). FeS always forms at 718 K due to the reaction of iron metal with H_2S . The pressure-independence of this reaction follows from simple mass action arguments applied to the reaction



and assumes that metallic iron is available in the equilibria to react with the buffer gas H_2S .

At $\sim 2000 \text{ K}$, chromium exists predominantly in the form of gaseous CrH, but is converted in large part into the metal near 1560 K ($\pm 15 \text{ K}$, depending upon the pressure (gravity)). Near and below 1500 K, the dominant compound of chromium is solid Cr_2O_3 . At 1500 K, CrH exists, but involves only a few percent by number of the available element.

Hence, the disappearance of CrH (g) occurs around 1400–1500 K.

At temperatures below ~ 200 K, NH_3 condenses into clouds. Such clouds are seen in Jupiter and Saturn, but as implied in Figure 2 they may be present in the lowest-mass EGPs with T_{eff} s below ~ 300 K.

The ratio $\{\text{Ti}_{\text{con}}\}/\text{TiO}$ on Figure 2 indicates where the abundance of one or more titanium condensates is equal to that of the gas-phase TiO, since the first titanium condensate to form with decreasing temperature depends upon the pressure. Note that for pressures corresponding to red dwarf atmospheres, perovskite, CaTiO_3 , is the first titanium condensate to appear, whereas for sub-stellar objects this is replaced by Ti_3O_5 . As indicated in Figure 2, there is a range of pressures where both form. At lower temperatures, the first titanium condensate to form changes into other compounds (Ti_3O_5 , Ti_2O_3 , Ti_4O_7 , and MgTi_2O_5). Equilibrium abundance profiles for these species for various models of Gl 229B are shown in Figures 11 and 12. The Ti transition sequence starting from ~ 2400 K to ~ 2100 K is quite general for substellar objects with T_{eff} s below ~ 2000 K. For T_{eff} s above ~ 2000 K, perovskite replaces Ti_3O_5 as the first condensed species into which TiO is transformed and titanium is depleted.

The main gas-phase species of vanadium and the first condensate to appear are both VO, and the curve on Figure 2 labeled by $\{\text{VO}\}/\text{VO}$ shows where these two phases have equal abundance. The condensed phase of VO first appears to the left of the curve. Abundance profiles for V compounds for a range of Gl 229B models are depicted in Figures 11 and 12. VO is depleted into solid VO, then into V_2O_3 , but its depletion sequence starts near 1800 K at lower temperatures than for titanium. Hence, we expect that in brown dwarfs and EGPs (and presumably in M dwarfs) first the abundance of gaseous TiO will decrease (near T_{eff} s of 2100 to 2400 K) and then (near 1800 K) the abundance of gaseous VO will decrease due to its depletion into solid VO. This depletion order should manifest

itself in the spectral sequence of cool objects.

3.2. Silicates, Phosphorus, Sodium, Potassium

In Figure 3, the condensates MgSiO_3 (enstatite), Mg_2SiO_4 (fosterite), and MgAl_2O_4 (spinel) are shown and are the most important condensates of magnesium, silicon, and aluminum. In the equilibrium calculations, these condensates are found to persist to lower temperatures, and unlike those of titanium and vanadium, do not change into other compounds. Figures 7 and 8 depict the equilibrium abundance profiles of enstatite and fosterite for the range of Gl 229B models. Figures 9 and 10 show the same for the more refractory silicates. Also included in Figures 3, 9, and 10 are the two main high-temperature condensates of sodium and potassium, $\text{NaAlSi}_3\text{O}_8$ (high albite) and KAlSi_3O_8 (high sanidine).

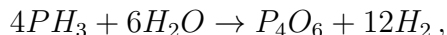
As indicated on Figures 9 and 10, the most refractory compounds are the calcium aluminum silicates (*e.g.*, akermanite), followed by the calcium magnesium (iron) silicates. These condensates can be found from temperatures of ~ 2300 K down to ~ 1800 K. Above ~ 2000 K, a major reservoir of Si is gaseous SiO (not shown in the figures), which is progressively sacrificed to form the refractories as the temperature decreases. Below 1800 K, among the classical refractories only spinel, enstatite, fosterite, and diopside ($\text{CaMgSi}_2\text{O}_6$) remain in abundance. In equilibrium, diopside is the low-temperature reservoir of calcium, while that of aluminum transitions from spinel to high albite back to spinel as the temperature decreases. The latter transition occurs below the minimum temperature shown in Figures 9 and 10. The aluminum-bearing compound, corundum (Al_2O_3), is not a major component of brown dwarf atmospheres. As Figure 3 demonstrates, enstatite and fosterite appear near the photospheres of brown and M dwarfs at temperatures from 1700 to 1900 K. In fact, as the relevant figures imply, classical silicate grains form in a temperature

range from 2400 K to 1500 K. This is just the T_{eff} transition regime between stars and brown dwarfs and serves to emphasize the importance of grain opacity in determining the properties of transition objects and in setting the T_{eff} and luminosity of the main sequence edge. Its role has yet to be precisely delineated, but Burrows *et al.* (1993) note that at the edge T_{eff} is decreased by ~ 250 K to ~ 1750 K when the approximate effects of grains are included.

At high temperatures, sodium and potassium are in monatomic form, but at temperatures of 1300 to 1500 K (Figures 3, 9, and 10) $\text{NaAlSi}_3\text{O}_8$ and KAlSi_3O_8 condense. Figure 4 depicts the $\text{Na}/\text{NaCl(g)}$ and $\text{K}/\text{KCl(g)}$ transition boundaries that occur in the 1000 K to 1500 K temperature range and near the photosphere for T_{eff} s of 1200 to 1400 K. Not shown on Figure 4, these chlorides condense below 800 K. Hence, as the temperature decreases, the major sodium species are first atomic Na, then gaseous NaCl and solid $\text{NaAlSi}_3\text{O}_8$, and finally solid NaCl. Potassium shows a similar sequence. The presence of condensed NaCl and KCl at low temperatures (below the inferred T_{eff} of Gl 229B !) is quite suggestive and we will return to this in §4.

Figures 9 and 10 depict representative abundance profiles for the dominant phosphorus compounds and Figure 3 depicts the major chemical transitions phosphorus undergoes. The $\text{PH}_3 \rightarrow \text{P}_4\text{O}_6 \rightarrow \text{Mg}_3\text{P}_2\text{O}_8$ transformations occur in the temperature range of 800 to 1200 K. The chemistry of phosphorus is particularly interesting, as the condensation temperature of $\text{Mg}_3\text{P}_2\text{O}_8$ (magnesium orthophosphate) is only weakly dependent upon pressure and forms very close to the photosphere of many of the depicted brown dwarf models. The predominant gas-phase species of phosphorus at about 1200 K is PH_3 (phosphine). Except at pressures above about 30 atmospheres, PH_3 is rapidly oxidized by H_2O to form the gas-phase oxide P_4O_6 , which becomes by far the dominant compound of phosphorus until $\text{Mg}_3\text{P}_2\text{O}_8$ condenses. At higher pressures, $\text{Mg}_3\text{P}_2\text{O}_8$ first condenses and

then the remaining gas-phase phosphorus forms the oxide. The curve on Figure 3 labeled $(\text{P}_4\text{O}_6 + \{\text{Mg}_3\text{P}_2\text{O}_8\})/\text{PH}_3$ indicates where the abundance of PH_3 is the same as the sum of the abundances of the oxide and the condensate, which except for the highest pressures where $\text{Mg}_3\text{P}_2\text{O}_8$ condenses first, is where the ratio $\text{P}_4\text{O}_6/\text{PH}_3$ is unity. Note that the phosphorus equilibrium can be represented by the reaction:



which involves more gas-phase molecules on the left-hand-side than the right. Hence, Le Chatelier’s Principle can be used to explain why the slope of the phosphorus curve is anomalously positive, unlike that of the other curves in Figure 3.

However, according to Borunov, Dorofeeva, & Khodakovsky (1995), the thermodynamic data for the gaseous species P_4O_6 in the JANAF tables may be in error, and may result in an overestimate of its abundance. In their work, they report a less negative value for the enthalpy of formation of P_4O_6 , which would be reflected in a lower abundance. We have been using the data from the JANAF tables, and find that with decreasing temperature P_4O_6 replaces phosphine, PH_3 , as the dominant gas-phase phosphorus-bearing compound below about 1100 K in brown dwarf atmosphere models, until the condensate magnesium orthophosphate, $\text{Mg}_3\text{P}_2\text{O}_8$, forms between about 800 and 900 K, as shown in Figure 3 (assuming other magnesium condensates are available to react with phosphorus-bearing species). It may be that the abundance of P_4O_6 is overestimated in our calculations. However, for a present-day Jupiter model, and other similar models, magnesium orthophosphate condenses near to or above the temperature at which the phosphorus chemistry of the gas phase switches over from being dominated by PH_3 to being dominated by P_4O_6 , so it appears that P_4O_6 may not in any case play an important role. In Figure 3, the curves indicating the phosphorus chemistry clearly show that at high pressures the condensation of $\text{Mg}_3\text{P}_2\text{O}_8$ overlaps with the formation of P_4O_6 .

3.3. Lithium, Cesium, Rubidium, Chlorine, Fluorine

Figure 4 depicts the atomic to gaseous chloride transitions for the alkali metals and compares them to model temperature–pressure profiles from Burrows *et al.* (1997) at 1 Gyr. Figures 13 and 14 show the abundance profiles for Li, Cs, and Rb species for various Gl 229B models. The chemistry of these metals is similar, but since the elemental abundances are quite different (Table 1), there is the natural ordering (Li, Rb, Cs) depicted in the figures. Lithium is in atomic form above ~ 1700 K, but is converted first into LiOH, then into LiCl at lower temperatures. Below ~ 700 K, in equilibrium lithium resides in LiAlO₂. Hence, at sufficiently low temperatures, the “lithium” test at 6708 Å is of no use. Below T_{eff}s of perhaps 1300 to 1600 K, atomic lithium will be depleted and the strength of the standard lithium line will abate. Below temperatures of 1200 K, the abundance of atomic lithium will be \sim one hundredth of solar. Interestingly, at these low T_{eff}s, spectral signatures of the chlorides may be detectable in the mid–infrared. The consequence of this is to nullify the standard lithium test for the majority of brown dwarfs and EGPs, unless they are caught early in their lives (*e.g.*, in young clusters) or are “massive” and near the transition edge.

Rubidium and cesium form the chloride as well, but at temperatures that are 200 to 300 K lower than does Li. Nevertheless, the alkali metals survive in atomic form to lower temperatures than do the other true metals. Since they are less refractory and survive in monatomic form for a longer stretch of temperature, the alkali metals should manifest themselves in the spectra of transition objects after the other metals (*e.g.*, Fe, Ca, Ti, V, Mg, Al) are depleted and rainout, as described above and in §4. Very approximately, the order of disappearance of the atom with decreasing temperature from ~ 1500 K to ~ 1200 K should be: Li, Na, Cs, Rb, K, with Cs, Rb, and K disappearing at about the same temperature. (Note that Na and K are depleted into high albite and sanidine as well.) Something like

this seems to be what is being observed by the 2MASS (Kirkpatrick *et al.* 1998) and DENIS (Tinney *et al.* 1998) collaborations in the spectra of newly-discovered substellar (?) and transition objects in the field.

From Figures 4, 13, and 14 we would predict that atomic cesium would be weak or non-existent in the spectrum of Gl 229B itself. However, two cesium lines are clearly visible in its spectrum (Oppenheimer *et al.* 1998). Along with the anomalous (see Figures 2, 5, and 6) detection of CO in the cold atmosphere of Gl 229B alluded to above, the atomic cesium detections may imply that its convective zone extends below 1500 K to ~ 1200 K and that some of its chemistry is not in equilibrium. In principle, grain and cloud opacities can extend the convective zone beyond the range theoretically predicted without them (Burrows *et al.* 1997). The necessity to include chemical kinetics in the convective zones will further complicate the theoretical treatment of brown dwarf atmospheres.

Due to its small abundance, fluorine is not a very important element, but its chemistry is similar to that of chlorine. In these calculations, most of fluorine is in HF, with much of the remainder being in the gas-phase alkali fluorides. Chlorine is combined in HCl, with much of the rest at low temperatures being in the gas-phase alkali metal chlorides.

4. Rainout

The equilibrium abundance calculations we presented in §3 are fiducial reference models in the study of the atmospheric compositions of brown dwarfs and EGPs, in general, and of Gl 229B, in particular. Tables 2a and 2b and Figures 2 through 14 summarize the results and the major trends. However, as demonstrated in the Gl 229B campaign and in attempts to fit its spectrum, there is strong evidence that heavy metals, such as Ca, Fe, Ti, V, Si, Al, and Mg, are depleted in Gl 229B’s atmosphere (Marley *et al.* 1996). In addition,

such depletions are manifest in the atmospheres of Jupiter and Saturn. This is altogether to be expected, since the grains that condense below temperatures of ~ 2500 K should form droplets and rain out of the atmosphere. This “rainout” will carry the condensate’s elements to depth. The lower boundary of the grain cloud deck should be near where the object’s temperature–pressure profile intersects the condensate’s “Clausius–Clapyron” lines (see Figures 2–4), but its upper boundary is more difficult to determine. The physical extent of the clouds is a function of the character of convection and the meteorology of the atmosphere. The droplet sizes are determined by the poorly–understood processes of nucleation, coagulation, and breakup. Furthermore, the high opacity of the grains can turn an otherwise radiative zone into a convective zone, and, thereby, influence the cloud extent and composition. In principle, if a convective zone were well–mixed and the chemical kinetics were suitably fast, the compositions in the convective zones would closely follow the equilibrium abundance patterns described in §3. However, the condensibles are likely to settle and concentrate at depth. In short, due to the low temperatures of substellar atmospheres, we would expect a variety of cloud layers with a variety of compositions both above and below their photospheres. Which clouds dominate is expected to be a function of the object’s effective temperature, gravity, and metallicity.

The equilibrium calculations are a straightforward guide in determining the likely cloud chemicals and layers as a function of depth (temperature). However, it is not known where the tops of these cloud decks will reside. The condensates that form from temperatures of ~ 2400 K to ~ 1400 K (*e.g.*, akermanite, spinel, Fe, enstatite, fosterite, the titanates, MnS, high albite) have in a Gl 229B column total grammages above a few gm cm^{-2} . The optical depth of a column of monodispensed grains is approximately

$$\tau \sim \frac{Pf}{\rho_0 g a} Q_{ext} \sim \frac{G}{\rho_0 a} Q_{ext}, \quad (4)$$

where P is the pressure at the base of the cloud layer of a given composition, f is the mixing ratio of the cloud particles, g is the gravity, Q_{ext} is the extinction parameter in Mie theory, G is the cloud grammage, ρ_0 is the density of a grain, and a is the grain radius. The term with P in it assumes that the atmosphere is completely depleted in the corresponding refractory down to the cloud base. From eq.(4), we can readily calculate that the predominantly silicate and iron cloud layers below the photosphere of Gl 229B are quite optically thick ($\geq 10^3$), the precise thickness depending crucially upon grain radius. Grain radii would have to exceed 1 cm to render these clouds transparent, whereas it is expected that the mean a will be below 100 μm (Lunine *et al.* 1989). Hence, these regions are expected to be more vigorously convective than would be expected without grain opacity and the convective zone may extend to lower pressures and temperatures. This phenomenon may help to explain the anomalous detections of Cs (Oppenheimer *et al.* 1998) and CO (Noll, Geballe, & Marley 1997) in Gl 229B, particularly if disequilibrium chemistry is involved, though a detached convective zone (Marley *et al.* 1996) may also be implicated.

However, the rainout of a high-temperature refractory will leave the upper regions of brown dwarf and EGP atmospheres depleted in the refractory’s constituent elements, in stoichiometric ratios. The lower-temperature chemical species will be assembled from the depleted elemental mixture. As a consequence, chemical abundances will be altered from the values assuming an Anders & Grevesse (1989) mixture at all altitudes (§3). We attempt to explore this process with a series of artificial “rainout” calculations in which we progressively sequester from the calculation the elements involved in grain formation. From some starting temperature that defines each exercise (either 1000, 1400, or 2000 K: trial 1, 2, or 3), every 200 K we deplete the atmosphere (in stoichiometric ratios) of the elements found in the chemical species that condense in that temperature interval. In the lower 200 K interval, we perform the equilibrium calculations with a composition depleted in the constituent elements of the higher temperature refractories. This simulates in a crude way

the progressive depletion and rainout of refractory elements from the entire atmosphere as we go down to lower temperatures (higher altitudes, lower pressures). For example, for trial 3, we progressively deplete from the atmosphere the constituents of the refractories formed at 2000 K, 1800 K, 1600 K, 1400 K, 1200 K, 1000 K, 800 K, and 600 K. For trial 1, we do the same for 1000 K, 800 K, and 600 K, but with an Anders & Grevesse mixture leave in equilibrium the layers at higher temperatures. A major motivation for this exercise is the identification of likely condensates in the *upper* atmosphere of Gl 229B, below temperatures of 1000 K, that may be implicated in the muting of the “optical” spectrum observed from $\sim 1 \mu\text{m}$ to $\sim 0.8 \mu\text{m}$ (Oppenheimer *et al.* 1998). The different trials represent our attempt to bracket the results. If this procedure consistently identifies specific low-temperature refractory compounds below ~ 1000 K at useful cloud grammages then we may have a reasonable hint at the culprits.

Tables 3a and 3b depict the results of these trials below 1000 K. The temperature–pressure profile used is for a Gl 229B model with a T_{eff} of 950 K and a gravity of 10^5 cm s^{-2} (Burrows *et al.* 1997). The species listed have condensed either in the 800–1000 K range (Table 3a) or in the 600–800 K range (Table 3b), after the corresponding depletions have been carried out at depth by the described procedure. Certain features are readily apparent. First, the grammages of the clouds formed at altitude are significantly below the few gm cm^{-2} for silicates at depth. This is encouraging, since only modest optical depths are needed to explain the shorter-wavelength Gl 229B data. From eq.(4), a grammage of only $10^{-5} \text{ gm cm}^{-2}$ with a particle radius of $0.1 \mu\text{m}$ provides close to unit optical depth. (Note that small particles are expected in radiative zones.) Second, the “abundant” low-temperature refractories are predominantly the chlorides and the sulfides. In particular, KCl, NaCl, NaF, and SiS_2 stand out, with SiS_2 dominating for trial 3. Without depletion, SiS_2 would not form in abundance, but progressive depletion starting at the highest temperatures is needed for it to become important. If SiS_2 forms, it does so around 743 K, whereas NaF

forms near 920 K, NaCl forms near 800 K, and KCl forms near 740 K. Be that as it may, the sodium and potassium salts emerge as cloud candidates in Gl 229B’s upper atmosphere, with grammages that may range from $\sim 10^{-4}$ to $\sim 4 \times 10^{-6}$ gm cm $^{-2}$. In trial 3, though the KCl cloud is thin, the SiS $_2$ is thick. These calculations suggest that thin clouds of non-silicate, low-temperature refractories can and do exist in the upper atmosphere of Gl 229B. Furthermore, they may also reside in the atmospheres of brown dwarfs with T_{eff} below about 1400 K (?). Hence, it is expected that many cloud layers with different compositions are formed both above and below the photospheres of brown dwarfs and EGPs. At times, from the lowest effective temperatures up, clouds of either NH $_3$ ($T_{\text{eff}} \leq 250$ K), H $_2$ O ($T_{\text{eff}} \leq 400$ K), chlorides, sulfides, iron, or silicates should be found in these exotic substellar and late M dwarf atmospheres.

5. Discussion and Conclusions

We have explored in detail the abundance profiles and compositions expected in the atmospheres of brown dwarfs and EGPs. In chemical equilibrium, the major reservoirs of the dominant elements shift with pressure and, most importantly, with temperature in ways reflected in Figures 2 through 14 and in Tables 2a and 2b. Unlike in any other stellar context, chemistry and molecules assume a central role in determining the character of the atmospheres of substellar objects. As the temperature decreases with increasing height in such an atmosphere, molecules not encountered in M dwarfs or in standard stellar atmospheres form. At the higher temperatures, the standard refractories, such as the silicates, spinel, and iron, condense out into grain clouds which by their large opacity lower the T_{eff} and luminosity of the main sequence edge (Burrows *et al.* 1993) and alter in detectable ways the spectra of objects around the transition mass (Jones & Tsuji 1997). As T_{eff} decreases below that at the stellar edge, the classical refractories are buried

progressively deeper below the photosphere and less refractory condensates and gas-phase molecules come to dominate (Marley *et al.* 1996; Burrows *et al.* 1997).

Below temperatures of ~ 1500 K, our calculations demonstrate and confirm that the alkali metals, which are not as refractory as Fe, Al, Ca, Ti, V, and Mg, emerge as important atmospheric and spectral constituents. At still lower temperatures, chlorides and sulfides appear, some of which will condense in the cooler upper atmosphere and form clouds that will affect emergent spectra and albedos. Cloud decks of many different compositions at many different temperature levels are expected, depending upon T_{eff} (and weakly upon gravity). We expect that clouds of chlorides and sulfides (not silicates), at temperature levels below ~ 1000 K, are responsible for the steeper slope observed in the spectrum of Gl 229B at the shorter wavelengths (Oppenheimer *et al.* 1998). At slightly higher temperatures, MnS, ZnS, NaAlSi₃O₈, KAlSi₃O₈, V₂O₃, Mg₃P₂O₈, and MgTi₂O₅ may play a role, but only if their constituents are not scavenged into more refractory compounds and rained out deeper down.

As T_{eff} decreases (either as a given mass cools or, for a given age, as we study objects with lower masses), the major atmospheric constituents of brown dwarfs and EGPs change. This change is reflected in which spectral features are most prominent and in the albedos of substellar objects near their primaries. Hence, specific mixes of atoms, molecules, and clouds can serve as approximate T_{eff} and temperature indicators and a composition scale can be established. In order to do this definitively, synthetic spectra with the atmospheres we have calculated are required. However, the composition trends we have identified are suitably dramatic that reasonable molecular indicators of spectral type can be suggested. A workable sequence might be: TiO disappears (at 2300–2000 K), refractory silicates and Fe(c) appear (at 2300–2000 K), Mg₂SiO₄ appears (at 1900 K), VO(g) disappears (at 1700–1900 K), MgSiO₃ appears (at 1700 K), silicates rainout (at ~ 1400 K (?)), CrH

disappears (~ 1400 K), $\text{Li} \rightarrow \text{LiCl}$ (≤ 1400 K), $\text{CO} \rightarrow \text{CH}_4$ (1200–1500 K), (Rb,Cs,K) \rightarrow chlorides (≤ 1200 K), $\text{PH}_3 \rightarrow (\text{P}_4\text{O}_6, \text{Mg}_3\text{P}_2\text{O}_8)$ (≤ 1000 K), formation of NaF, NaCl, and KCl clouds and various sulfide clouds (~ 700 – 1100 K), $\text{N}_2 \rightarrow \text{NH}_3(\text{g})$ (~ 700 K), $\text{H}_2\text{O}(\text{g}) \rightarrow \text{H}_2\text{O}(\text{c})$ (~ 350 K), and $\text{NH}_3 \rightarrow (\text{NH}_3(\text{c}), \text{NH}_4\text{SH}(\text{c}))$ (~ 200 K).

Disequilibrium chemistry and convection and differences in the spectroscopic strengths of the various indicators will no doubt partially alter the T_{eff} order of this spectral scale. Note that objects with T_{eff} s higher than the temperatures quoted above may nevertheless, because of the lower temperatures that can be achieved at lower optical depths, manifest lower-temperature compounds and/or transitions in their atmospheres and spectra. Gl 229B with a T_{eff} of ~ 950 K is a case in point, if lower-temperature chloride and sulfide refractories are to be invoked to explain its spectrum. How much higher the appropriate T_{eff} should be for a given chemical transition to be fully manifest will depend upon consistent atmosphere models. Clearly, the above temperatures for the appearance or disappearance of species should be used with great caution when estimating T_{eff} . Very crudely, the “L” spectral type suggested by Kirkpatrick *et al.* (1998) would correspond to T_{eff} s between about ~ 1500 K and ~ 2200 K. None but the youngest and most massive brown dwarfs and only the very youngest EGPs could have this proposed spectral designation. Most brown dwarfs and EGPs will be of an even later spectral type, yet to be coined, a spectral type that would include Gl 229B.

In the future, more consistent atmospheres and a detailed spectral sequence need to be calculated. Furthermore, we need to expand our inventory of possible compounds and explore the effect of metallicity. Importantly, credible cloud models, incorporating realistic grain size distributions and their altitude dependence, will be required to explain the spectral and photometric data on brown dwarfs and extrasolar giant planets that has already been obtained and that can be anticipated in the near future. Given the ambiguities

in cloud physics and theoretical meteorology, new observations will be crucial to educate and guide theory concerning the true nature of substellar atmospheres. Nevertheless, it is clear that brown dwarfs and giant planets occupy an exciting new realm of science midway between astronomy and planetary studies in which new insights and for which new tools must be developed. The theoretical study of substellar objects with T_{eff} s between those of Jupiter and the stars has only just now begun in earnest.

We thank Mark Marley, Bill Hubbard, Jonathan Lunine, David Sudarsky, Didier Saumon, Shri Kulkarni, Ben Oppenheimer, Jim Liebert, Davy Kirkpatrick, France Allard, Gilles Chabrier, and Tristan Guillot for a variety of useful contributions. This work was supported under NASA grants NAG5-7499, NAG5-7073, and NAG5-2817.

REFERENCES

- Allard, F., Hauschildt, P.H., Baraffe, I. & Chabrier, G. 1996, *ApJ*, 465, L123
- Anders, E. & Grevesse, N. 1989, *Geochim. Cosmochim. Acta*, 53, 197
- Barin, I. 1995, “Thermochemical Data of Pure Substances,” VCH, Verlagsgesellschaft bmH. Weinheim, Germany.
- Besmann, T.M. 1977, “SOLGASMIX-PV - A computer Program to Calculate Equilibrium Relationships in Complex Chemical Systems,” Oak Ridge National Laboratory Report TM-5775.
- Borunov, S., Dorofeeva, V. & Khodakovsky, I. 1995, *Icarus*, 113, 460
- Burrows, A., Hubbard, W.B., & Lunine, J.I. 1989, *ApJ*, 345, 939
- Burrows, A., Hubbard, W.B., Saumon, D., & Lunine, J.I. 1993, *ApJ*, 406, 158
- Burrows, A., Saumon, D., Guillot, T., Hubbard, W.B., & Lunine, J.I. 1995, *Nature*, 375, 299
- Burrows, A., Marley M., Hubbard, W.B. Lunine, J.I., Guillot, T., Saumon, D. Freedman, R., Sudarsky, D. & Sharp, C. 1997, *ApJ*, 491, 856
- Butler, R. P. & Marcy, G. W. 1996, *ApJ*, 464, L153
- Chabrier, G. *et al.* 1998, to be published in the proceedings of the first Euroconference on *Stellar Clusters and Associations*, held in Los Cancajos, La Palma, Spain, May 11–15, ed. R. Rebolo, V. Sanchez-Bejar, and M.R. Zapatero-Osorio
- Chase, M.W., 1982, “JANAF Thermodynamic Tables”, Magnetic Tape Version (Midland, MI: Dow Chemical Co.).
- Chase, M.W., Davies, C.A., Downey, J.R., Frurip, D.J., McDonald, R.A., & Syverud, A.N. 1985, *J. Phys. Chem. Ref. Data*, 14, Suppl.1, 1

- Cochran, W.D., Hatzes, A.P., Butler, R.P., & Marcy, G. 1997, *ApJ*, 483, 457
- Comeron, F., Rieke, G.H., Burrows, A., & Rieke, M.J. 1993, *ApJ*, 416, 185
- Delfosse, X., Tinney, C.G., Forveille, T., Epchtein, N., Bertin, E., Borsenberger, J., Copet, E., De Batz, B., Fouqué, P., Kimeswenger, S., Le Bertre, T., Lacombe, F., Rouan, D., & Tiphène, D. 1997, *Astron. Astrophys.*, 327, L25 (DENIS)
- Eisenberg, D. & Kauzmann, W. 1969, “The Structure and Properties of Water,” (New York: Oxford University Press)
- Fegley, B. & Lodders, K. 1996, *ApJ*, 472, L37
- Guillot, T., Saumon, D., Burrows, A., Hubbard, W.B., Lunine, J.I., Marley, M., & Freedman, R. 1997, in *Astronomical and Biochemical Origins and the Search for Life in the Universe*, eds. C. Cosmovici, S. Bowyer, and D. Wertheimer, p. 343
- Jones, H.R.A. & Tsuji, T. 1997, *ApJ*, 480, L39
- Kirkpatrick, J.D., Beichman, C.A., & Skrutskie, M.F. 1997, *ApJ*, 476, 311
- Kirkpatrick, J.D., Reid, I.N., Liebert, J., Cutri, R.M., Nelson, B., Beichman, C.A., Dahn, C.C., Monet, D.G., Skrutskie, M.F., & Gizis, J. 1998, in preparation
- Latham, D. W., Mazeh, T., Stefanik, R.P., Mayor, M., & Burki, G. 1989, *Nature*, 339, 38
- Lewis, J.S. 1969, *Icarus* 10, 365
- Lunine, J.I., Hubbard, W.B., Burrows, A., Wang, Y.P., & Garlow, K. 1989, *ApJ*, 338, 314
- Marcy, G. W. & Butler, R. P. 1996, *ApJ*, 464, L147
- Marley, M.S., Saumon, D., Guillot, T., Freedman, R.S., Hubbard, W.B., Burrows, A. & Lunine, J.I. 1996, *Science*, 272, 1919
- Marley, M.S., Gelino, C., Stephens, D., Lunine, J.I., & Freedman, R. 1998, submitted to *ApJ*

- Matthews, K., Nakajima, T., Kulkarni, S.R., & Oppenheimer, B.R. 1996, *AJ*, 112, 1678
- Mayor, M. & Queloz, D. 1995, *Nature*, 378, 355
- Nakajima, T., Oppenheimer, B.R., Kulkarni, S.R., Golimowski, D.A., Matthews, K. & Durrance, S.T. 1995, *Nature*, 378, 463
- Noll, K., Geballe, T.R., & Marley, M., 1997, *ApJ*, 489, 87
- Oppenheimer, B.R., Kulkarni, S.R., Matthews, K., & Nakajima, T. 1995, *Science*, 270, 1478
- Oppenheimer, B.R., Kulkarni, S.R., Matthews, K., & van Kerkwijk, M.H. 1998, submitted to *ApJ*
- Robie, R.A. & Waldbaum, D.R. 1968, *US Geolog. Survey Bull.*, No. 1259
- Sharp, C.M. 1985, “Molecular Dissociation Functions Obtained from Thermodynamic and Spectroscopic Data”, in *Molecular Astrophysics*, ed. G.H.F.Diercksen, W.F.Huebner and P.W.Langhoff, NATO ASI Series, Mathematical and Physical Sciences, 157, 661
- Sharp, C.M. & Huebner, W.F. 1990, *Ap.J. Suppl. Ser.* 72, 417
- Sharp, C.M. & Huebner, W.F. 1993, “Molecular Equation of State with Condensation Code for Astrophysical Applications”, Southwest Research Institute Report 93-1, Texas.
- Terebey, S. *et al.* 1998, in preparation
- Tinney, C.G., Delfosse, X., & Forveille, T. 1997, *ApJ*, 490, L95 (DENIS)
- Tinney, C.G., Delfosse, X., Forveille, T. & Allard, F. 1998, *Astron. Astrophys.* , submitted
- Tsuji, T. 1973, *Astron. Astrophys.* , 23, 411
- Tsuji, T., Ohnaka, W., Aoki, W., & Nakajima, T. 1996, *Astron. Astrophys.* , 308, L29
- Turkdogan, E.T. 1980, “Physical Chemistry of High Temperature Technology,” US Steel Corp., (New York: Academic)

Weast, R.C. & Astle, M.J. 1980, “CRC Handbook of Chemistry and Physics,” CRC Press, Inc.

White, W.B., Johnson, W.M. & Dantzig, G.B. 1958, J. Chem. Phys., 28, 751

Zapatero-Osorio, M.R., Rebolo, R., & Martin, E.L. 1997, Astron. Astrophys. , 317, 164

Fig. 1.— Plot of the temperature–pressure profiles for models with masses of 5, 10, 20 and 40 M_J at ages of 0.1, 1, and 10 Gyr shown as dash–dotted, dashed, and solid curves, respectively. The positions of the photospheres for each model are shown as solid circles. The four horizontal lines connect the positions of the photospheres for models with the same mass. (The lowest mass (5 M_J) line–of–photospheres is at the top.) The masses in M_J s label the corresponding profiles. At 0.1 Gyr, there are only two models and labels, one for 5 M_J and one for 10 M_J . Note that at high pressures the model for 5 M_J at 1 Gyr overlaps with that for 40 M_J at 10 Gyr.

Fig. 2.— Condensation or chemical transformation boundaries for major species in temperature–pressure space. Superposed on the figure are atmospheric profiles, shown as solid curves, from Figure 1 for a number of giant planet and brown dwarf models with an age of 1 Gyr. The models of Burrows *et al.* (1997) were employed. Included are a present–day Jupiter profile and 1 Gyr adiabats for M dwarf models with masses of 0.08, 0.09 and 0.115 M_\odot ($1M_\odot = 1047M_J$). The black–filled circles indicate the location of the photosphere. The region to the left of a circle spans the atmosphere above the photosphere. Note that for the red dwarfs we have extrapolated temperatures somewhat above the height of the photosphere assuming an adiabatic law. In reality, this is in the radiative regime and the profile pressures at a given temperature should be lower, as are those for the substellar models. Chemical boundary curves indicate when a condensed species forms or when a ratio of abundances is unity. The condensates are written in braces “{ }” to distinguish them from gas–phase species. A condensate forms on and immediately to the left of each indicated curve, and in some cases may disappear into another phase at lower temperatures, but is not shown. The curve labeled by a ratio, such as CH_4/CO , indicates where these two species have equal abundances, with the ratio greater than unity to the left. See the text for further explanations.

Fig. 3.— The same as Figure 2, except important silicates, spinel, and phosphorus compounds are plotted. As in Figure 2, the ratios or abundances increase to the left. See text for details.

Fig. 4.— The same as Figure 2, but showing the loci of points where the partial pressures of the gas-phase alkali metal chlorides are equal to those of the corresponding metal vapors. The chlorides exist on the low-temperature side of the metal/chloride boundaries. With the exception of lithium, which has some characteristics similar to an alkaline-earth element, the formation of the chloride occurs at temperatures that increase with increasing molecular weight.

Fig. 5.— Plots of the abundance profiles for several of the most abundant chemical species, H_2O , CH_4 , CO , NH_3 and N_2 , for brown dwarf models with an effective temperature of 950 K, but with the gravities of 300, 1000 and 3000 m s^{-2} . The temperature of 950 K is chosen because it is near that of the brown dwarf Gl 229B. Temperature–pressure profiles for the underlying dwarf models are implicit and are from Burrows *et al.* (1997). Each curve is a plot of \log_{10} of the number fraction of a particular species out of all species, including any condensates, as a function of level temperature. An increase in temperature generally corresponds to an increase in pressure and depth. Each set of curves is labeled by the chemical species H_2O , CH_4 , CO , NH_3 and N_2 , and the numbers 300, 1000 and 3000 correspond to each model’s gravity. For example, the set of curves labeled CO and 300, 1000, and 3000 show the profiles for CO for the three models. The two most abundant species, H_2 and He , would be above the top of the figure and are not plotted. For clarity, the profile for CO is shown as a dashed curve and the label of 1000 is omitted from the plots of H_2O and N_2 . The vertical line at 950 K shows the position of the photosphere. The condensates are identified here and in the following figures by being enclosed in braces, $\{\}$.

Fig. 6.— The same as Figure 5 for the same five species, but for five models with the effective

temperatures of 800, 850, 900, 950 and 1000 K, for a fixed gravity of 1000 m s^{-2} . Each set of curves is labeled by the species, with 800 and 1000 indicating the coolest and hottest models in the sequence, with the other models lying in between. The five photospheric temperatures are shown as short tick marks at the bottom of the figure.

Fig. 7.— The abundances of the gas-phase species H_2S , together with the condensates Fe, FeS, MgSiO_3 and Mg_2SiO_4 , are plotted for the effective temperature of 950 K, but with the gravities of 300, 1000 and 3000 m s^{-2} , as in Figure 5. As the abundances of H_2S and FeS are independent of the model, the numbers labeling the gravities are omitted.

Fig. 8.— The same five species are plotted as in Figure 7, but for the five models with fixed gravity and varying effective temperature used in Figure 6.

Fig. 9.— The abundances for $\text{NaAlSi}_3\text{O}_8$, KAlSi_3O_8 , MgAl_2O_4 , $\text{Mg}_3\text{P}_2\text{O}_8$, P_4O_6 , PH_3 , MnS, $\text{CaMgSi}_2\text{O}_6$, $\text{Ca}_2\text{MgSi}_2\text{O}_7$, and $\text{Ca}_2\text{Al}_2\text{SiO}_7$, for the gravities and effective temperature of Figure 5. For clarity, different line thicknesses are used. This figure includes some of the refractory silicates not plotted in the previous figures. From right to left, corresponding to decreasing temperature, the first condensate shown is $\text{Ca}_2\text{Al}_2\text{SiO}_7$, identified by the thick curves. Only the 3000 m s^{-2} gravity model is labeled. The thinner curves labeled “300” and “3000” at the top are for MgAl_2O_4 , and continue on to lower temperatures. The next set of thinner curves on either side of 2000 K refer to the appearance of $\text{Ca}_2\text{MgSi}_2\text{O}_7$, for which the 300 and 1000 models are labeled immediately to the left. The three following curves which rise to above -5.5 in the ordinate below 1900 K refer to the appearance of $\text{CaMgSi}_2\text{O}_6$, with the accompanying curves of the previous species indicating its disappearance. The remaining set of curves at lower temperatures are clearly identified by at least one of the models.

Fig. 10.— The same ten species shown in Figure 9, with the same line thickness, are plotted for models with effective temperatures of 800, 850, 900, 950 and 1000 K, for a fixed gravity

of 1000 m s^{-2} , as in Figure 6. The first condensate to be plotted to the right is $\text{Ca}_2\text{Al}_2\text{SiO}_7$, as in Figure 9, and is for the 800 K model.

Fig. 11.— The titanium and vanadium condensates, MgTi_2O_5 , Ti_4O_7 , Ti_2O_3 , CaTiO_3 , V_2O_3 and VO , together with their most important gas-phase species, TiO and VO , are plotted for the three different gravity models depicted in Figure 5 and for an effective temperature of 950 K . Note that with decreasing temperature, the highest temperature condensate, Ti_3O_5 , changes into Ti_2O_3 below 1900 K for the two higher gravity models, but for the lowest 300 m s^{-2} model Ti_3O_5 temporarily changes into CaTiO_3 above 2000 K in a range of about 100 K , before changing back into the high temperature condensate. As with the other models, this then changes into Ti_2O_3 below 1900 K .

Fig. 12.— The abundances of the same titanium and vanadium species depicted in Figure 11 are plotted for models with effective temperatures of $800, 850, 900, 950$ and 1000 K , for a fixed gravity of 1000 m s^{-2} , as in Figure 6. Note that in these models CaTiO_3 does not form.

Fig. 13.— The abundances of lithium, rubidium, cesium and their most abundant compounds for an effective temperature of 950 K and the three gravities employed in Figure 5. At the lowest temperatures plotted, the condensate RbCl forms, with the 300 m s^{-2} model being labeled.

Fig. 14.— The abundances of the same species depicted in Figure 13 are plotted for models with effective temperatures of $800, 900,$ and 1000 K , for a fixed gravity of 1000 m s^{-2} , as in Figure 6. We show a restricted set of curves because the results are only weakly dependent on effective temperature.

Table 1. Anders and Grevesse (1989) solar abundances [†]

Element	Abundance	Element	Abundance
H	9.10×10^{-1}	Ni	1.61×10^{-6}
He	8.87×10^{-2}	Cr	4.40×10^{-7}
O	7.76×10^{-4}	P	3.39×10^{-7}
C	3.29×10^{-4}	Mn	3.11×10^{-7}
Ne	1.12×10^{-4}	Cl	1.71×10^{-7}
N	1.02×10^{-4}	K	1.23×10^{-7}
Mg	3.49×10^{-5}	Ti	7.83×10^{-8}
Si	3.26×10^{-5}	Co	7.34×10^{-8}
Fe	2.94×10^{-5}	F	2.75×10^{-8}
S	1.68×10^{-5}	V	9.56×10^{-9}
Ar	3.29×10^{-6}	Li	1.86×10^{-9}
Al	2.77×10^{-6}	Rb	2.31×10^{-10}
Ca	1.99×10^{-6}	Cs	1.21×10^{-11}
Na	1.87×10^{-6}		

[†]The elements are given as fractions by number in order of decreasing abundance.

Table 2a. The most important species associated with each element †

Element	Major Chemical Species
H	H ₂
He	He
Li	Li LiCl LiF <u>LiAlO₂</u>
C	CO CH ₄
N	N ₂ NH ₃ <u>NH₃</u>
O	H ₂ O CO <u>H₂O</u>
F	HF LiF NaF KF RbF CsF <u>Na₃AlF₆</u> <u>LiF</u>
Ne	Ne
Na	Na NaCl <u>NaCl</u> <u>NaAlSi₃O₈</u> <u>Na₃AlF₆</u>
Mg	Mg MgH <u>MgSiO₃</u> <u>Mg₂SiO₄</u> <u>MgAl₂O₄</u> <u>CaMgSi₂O₆</u> <u>Ca₂MgSi₇O₇</u> <u>Mg₃P₂O₈</u> <u>MgTi₇O₅</u>
Al	Al AlH AlOH Al ₂ O <u>Al₂O₃</u> <u>MgAl₂O₄</u> <u>Ca₂Al₂SiO₇</u> <u>NaAlSi₃O₈</u> <u>KAlSi₃O₈</u> <u>Na₃AlF₆</u> <u>LiAlO₂</u>
Si	SiO <u>MgSiO₃</u> <u>Mg₂SiO₄</u> <u>Ca₂Al₂SiO₇</u> <u>Ca₂SiO₄</u> <u>CaMgSi₂O₆</u> <u>Ca₂MgSi₇O₇</u> <u>NaAlSi₃O₈</u> <u>KAlSi₃O₈</u> <u>MnSiO₃</u>
P	PH ₃ P ₄ O ₆ PN <u>Mg₃P₂O₈</u>
S	H ₂ S SH SiS <u>MnS</u> <u>FeS</u> <u>NH₄SH</u>

†The underlined species are condensates and the gas-phase species are given first. Otherwise, the order of the species is generally unimportant, though some condensates of less importance are given last.

Table 2b. Continuation of the listing of the most important species associated with each element †

Element	Major Chemical Species
Cl	HCl LiCl NaCl KCl RbCl KCl AlCl MgCl CaCl <u>NaCl</u> <u>RbCl</u> <u>CsCl</u>
Ar	Ar
K	K KCl <u>KAlSi₃O₈</u>
Ca	Ca CaH CaOH <u>Ca₂Al₂SiO₇</u> <u>Ca₂SiO₄</u> <u>Ca₂MgSi₂O₇</u> <u>CaMgSi₂O₆</u>
Ti	Ti TiO <u>Ti₃O₅</u> <u>Ti₂O₃</u> <u>Ti₄O₇</u> <u>MgTi₂O₅</u> <u>CaTiO₃</u>
V	V VO <u>VO</u> <u>V₂O₃</u> <u>VN</u>
Cr	Cr CrH <u>Cr</u> <u>Cr₂O₃</u>
Mn	Mn MnH <u>MnS</u> <u>MnSiO₃</u>
Fe	Fe FeH <u>Fe</u> <u>FeS</u>
Co	Co <u>Co</u>
Ni	Ni NiH <u>Ni</u>
Rb	Rb RbCl RbF <u>RbCl</u>
Cs	Cs CsCl CsF <u>CsCl</u>

†The underlined species are condensates and the gas-phase species are given first. Otherwise, the order of the species is generally unimportant, though some condensates of less importance are given last.

Table 3a. Inferred cloud grammages (g cm^{-2}) for species that condense between 1000 and 800 K for the three rainout trials[†]

Condensate	A1	A2	A3	Grammage 1	Grammage 2	Grammage 3
MnO	927			2.09×10^{-10}		
FeS	875			6.90×10^{-11}		
NaF		924			<u>2.01×10^{-5}</u>	
Ni ₃ S ₄		922			1.26×10^{-9}	
Fe ₃ O ₄		921			2.14×10^{-8}	
Co ₃ O ₄		836			1.17×10^{-8}	
NaCl		825			<u>6.74×10^{-5}</u>	
Li ₂ O		800			5.53×10^{-9}	
CaCl ₂			863			2.45×10^{-8}
Fe ₂ O ₃			862			1.18×10^{-7}
NiS ₂			835			1.15×10^{-7}

[†]A1, A2 and A3 are the temperatures in Kelvin when the condensate first appears for the first, second, and third rainout trials, respectively.

Table 3b. Inferred cloud grammages (g cm^{-2}) for species that condense between 800 and 600 K for the three rainout trials[†]

Condensate	A1	A2	A3	Grammage 1	Grammage 2	Grammage 3
NaCl	776		701	$\underline{1.04 \times 10^{-5}}$		2.44×10^{-7}
KCl	730	740	728	$\underline{4.62 \times 10^{-6}}$	$\underline{3.68 \times 10^{-5}}$	$\underline{4.20 \times 10^{-6}}$
LiF	700			2.68×10^{-7}		
RbCl	613		613	4.94×10^{-8}		4.94×10^{-8}
Mn		768	768		2.16×10^{-9}	2.12×10^{-9}
LiOH		745			3.15×10^{-7}	
Fe ₂ O ₃		726			1.72×10^{-10}	
MgF ₂		636			5.77×10^{-10}	
KF		605			5.03×10^{-9}	
SiS ₂			743			$\underline{4.13 \times 10^{-3}}$
Co ₃ O ₄			684			5.52×10^{-9}
LiCl			638			2.63×10^{-7}
CaF ₂			627			1.77×10^{-10}
MgCl ₂			615			8.85×10^{-10}

[†]A1, A2 and A3 are the temperatures in Kelvin when the condensate first appears for the first, second, and third rainout trials, respectively.

